JA

ISSN 1340-3745

ICRR

ICRR-Report-354-96-5

Azimuthally controlled observation of heavy cosmic-ray primaries by means of the balloon-borne emulsion chamber

E. Kamioka, M. Hareyama, M. Ichimura, Y. Ishihara,
T. Kobayashi, H. Komatsu, S. Kuramata, K. Maruguchi,
H. Matsutani, A. Mihashi, H. Mito, T. Nakamura,
H. Nanjo, T. Ouchi, T. Ozawa, T. Shibata,
H. Sugimoto and Z. Watanabe

(January, 1996)

Submitted to Astroparticle Physics

INSTITUTE FOR COSMIC RAY RESEARCH
UNIVERSITY OF TOKYO
3-2-1 Midori-cho, Tanashi, Tokyo 188, Japan

Azimuthally controlled observation of heavy cosmic-ray primaries by means of the balloon-borne emulsion chamber*

E. Kamioka[d], M. Hareyama[a], M. Ichimura[a], Y. Ishihara[d], T. Kobayashi[d], H. Komatsu[a], S. Kuramata[a], K. Maruguchi[d], H. Matsutani[b], A. Mihashi[d], H. Mito[a], T. Nakamura[a], H. Nanjo[a], T. Ouchi[e], T. Ozawa[a], T. Shibata[d], H. Sugimoto[f] and Z. Watanabe[c]

[a] Department of Physics, Hirosaki University, Hirosaki, Japan

[b] Faculty of Medicine, Hirosaki University, Hirosaki, Japan

[c] Aomori University, Aomori, Japan

[d] Department of Physics, Aoyama Gakuin University, Tokyo, Japan

[e] Institute for Cosmic Ray Research, University of Tokyo, Tokyo, Japan

[f] Syonan Institute of Technology, Kanagawa, Japan

ABSTRACT

We have exposed an emulsion chamber with the area of 1.22 m^2 on board the balloon at an atmospheric depth of 8.9 g/cm^2 for 15.8 h, which has been azimuthally controlled within the accuracy of $\Delta\phi = 0.5°$. With use of the east-west asymmetry effect of arriving cosmic-ray primaries, we can obtain the energy spectra for individual elements in the kinetic energy range from a few GeV/nucleon up to $\sim$ 15 GeV/nucleon. We present also the energy spectra obtained by the opening-angle method for the higher energy region, 5 $\sim$ 1000 GeV/nucleon, for the elements not lighter than silicon.

We find the energy spectra obtained by the former method continue smoothly to those obtained by the latter, indicating that the energy determination using the opening-angle method is performed correctly. We compare also the present results with those obtained by the previous work. We find that the iron flux is in nice agreement with that obtained by the previous observation, the differential spectral index being constant, $\sim$ 2.5, up to a few TeV/nucleon, while in the case of silicon component, it is $\sim$ 2.7 for 10 $\sim$ 1000 GeV/nucleon in this work, significantly harder than the previous one, $\sim$ 2.9.

We also report the flux of sub-iron component and its abundance ratio to the iron component. We find the abundance ratio of [Z=21-25]/iron is slightly less than those obtained previously in the higher energy region, $\gtrsim$ 100 GeV/n.

* This work is supported partially by ICRR, University of Tokyo (E25, 1994 and E40, 1989)

1 Introduction

We have exposed twice a new type of emulsion chamber on board the balloon with extensive use of the screen-type X-ray film (hereafter called SXF), which were launched from the Sanriku Balloon Flight Center ([N, E] = [39.2°, 141.8°]) of Institute of Space and Astronautical Science (ISAS), Japan, in May 1989 and in May 1991. The result of the first experiment in 1989 has been already reported in detail in the reference [1], and the present work is focused to the second one.

Since the emulsion chamber exposed in 1991 has been azimuthally controlled, we can estimate the energy spectrum in the region of $2 \sim 15$ GeV/nucleon with use of the east-west asymmetry effect (hereafter called E-W effect) of arrival cosmic-rays. Although the energy region is not so high, the flux measurement using the E-W effect is quite simple and reliable, as we can regard the terrestrial magnetic field as a giant magneto-spectrometer. One should remark further that *all* tracks recorded on SXF are used for the flux measurement regardless of their interactions in the chamber, resulting in rich statistics, while the opening-angle method is applicable only for those interacting in the target layer, reducing statistics.

Of course, in order to do so, we have to perform in advance extensive numerical calculations of the cut-off energy E_c for various arrival directions (θ, ϕ). We have developed a numerical method, excellent in both the reliability and the speed, and apply it for the present experiment. So it is very interesting and important to compare the flux value obtained by the E-W effect with those by the opening-angle method.

Another merit of the application of the E-W effect for cosmic-ray intensity measurement is to eliminate the detection-loss bias for the low energy region, $\lesssim 10$ GeV/nucleon, which has often appeared in the opening-angle method. That is, as mentioned in ref.

[1], it is sometimes difficult to detect a nuclear interaction with wide-opening angle of fragments, corresponding to low energy event, occurred in the acrylic target other than emulsion gel, particularly for lighter elements with large zenith angle such as the carbon $\sim$ silicon. On the other hand we don't need to worry about such a problem in the case of the flux measurement using the E-W effect. This means we can cover the flux measurement in the very wide energy from a few GeV/n to a few TeV/n using the same detector.

Naturally, the E-W effect is much more significant for arrival cosmic-rays with large zenith angle than for those with small one. Fortunately, the sensitivity of SXF is high enough also for inclined heavy tracks, so that we can detect the cosmic-ray heavy primaries for whole solid angle, detail of which is reported in ref. [2]. One should note that the sensitivity of CR-39 track detector is quite poor in detection for the inclined track[3], for instance detectable only for those with $\theta \lesssim 45°$ even in the case of iron track and much less in the case of lighter ones such as the carbon and silicon.

In sect. 2, we present the experimental procedure, and summarize the analysis and the results in sect. 3. Section 4 is reserved for discussion and summary.

2 Experimental procedure

2.1 Chamber structure

More thorough explanation can be found in ref. [1]. Here, only the essense and some new features are explained.

As shown in fig. 1, the chamber consists mainly of three parts. The top part is for trigger to require the cosmic ray track to go through these two layers. To get better angular resolution for arrival direction and reduce the interactions in this part, a styrofoam (SP) with the thickness of 2 mm is inserted between two SXF's.

The middle part is the acrylic target layer, where the thickness of each target is 1mm and the upper surface is coated with nuclear emulsion of 50 μm thickness (Em A) so that the nuclear fragments are easily detected. Total thickness of this module is 5.14cm in vertical, equivalent to 0.633 collision m.f.p. for the iron. The cosmic ray nuclei are detected in the form of dark spot recorded on SXF, detectable easily by naked eye for those heavier than oxygen. These numerous dark spots are followed down from the top layer to lower layers with use of the computer-guided large stage with CCD camera. The coordinate and the spot darkness of each track are automatically recorded every layer in the hard-disk of computer. The change of dark spot indicates the interaction of cosmic ray nucleus and the adjacent nuclear emulsion plate (Em B) is scanned to measure the opening angle of nuclear fragments for the energy determination.

The buttom part is the spacer to measure the opening angle of high energy nuclear fragment, each with 2mm (SP). The total thickness of the spacer is 8.4mm in vertical, and the path length between the middle point of the target and the bottom of the spacer is 3.4cm, thick enough for the spatial resolution of each fragment with a few TeV/n, taking the inclination effect into account.

We have made 8 blocks with the structure explained above, each having the geometrical size of 35.6cm(D) $\times$ 43.2cm(W) $\times$ 6.5cm(H). The principle of the chamber design is almost the same as that of '89 chamber, but the minor improvements are made to '91 chamber. The stainless plates were replaced by acrylic plates in the target layers to reduce the total weight of the chamber without significant loss of the interaction length for heavier nuclei. We removed CR-39 in this chamber because SXF is detectable for any inclined-heavy tracks, the characteristics of which are essential for the present study of the E-W effect.

2.2 Flight situation

The balloon was launched from the Sanriku Balloon Center of ISAS, May 28, 1991. The flight situation is summarized in table 1, together with '89 experiment for comparison. Figure 2 is the trajectry of the balloon, drifting to the northern latitude by $\sim 2°$, which is important to calculate the cut-off energy.

Notable thing in '91 exposure is the azimuthal control of the chamber with respect to the geomagnetic field. The chamber is oriented to a certain direction by the method called *azimuthal control by twisting suspension rope* developed by ISAS balloon division[4], monitoring the geomagnetic field. The control accuracy is $\sim 0.5°$ as shown in fig. 3, small enough for our purpose.

2.3 Event scanning

The scanning procedure is as follows:

1. Putting two SXF's of the trigger layers on the computer-guided large stage with CCD camera, aligned dark spots produced by one cosmic ray track are manually picked up and the position and darkness of these spots are stored on the computer disk.
2. Knowing the direction of tracks from the measurement on the trigger layers, all tracks are followed down to lower layers of SXF automatically.
3. While the tracks are followed down, the change of spot darkness on SXF is recorded as the candidate of the nuclear interaction. Nuclear fragments are looked for under the microscope using nuclear emulsion plate, corresponding to the place of the darkness change on SXF.

we detected 69236 tracks passing through the trigger layer. The charge of cosmic ray nucleus is determined by the darkness of spot recorded on SXF, similarly as in '89 analysis, details of which are discussed in refs. [1] and [2]. Figure 4 is the charge histogram obtained in this observation. One finds clearly the peak of primary elements such as oxygen, neon, ... Assuming the charge distribution is gaussian, the maximum likelihood method is applied to extract the width and height of the gaussian distribution for each element[1]. In fig. 4 are also drawn the fitting curves for individual elements. Charge resolution is 0.44 charge unit for silicon and 0.82 charge unit for iron, slightly improved for those obtained in the previous work, 0.46 and 0.97 charge unit respectively.

In this work, one of 8 blocks is fully analyzed for all interactions irrespective of the primary energy, and the rest 7 blocks are analyzed only for high energy events, producing fragments with narrow-opening angle, since one block is enough for collecting heavy primaries in the lower energy region. Statistics of individual elements passing through the trigger layer and the number of events interacting with the target are summarized in table 2. In table 3 is summarized the event number performing emission-angle measurement for the energy determination using the opening-angle method.

3 Analysis and results

3.1 Method of the energy-spectrum measurement

3.1.1. Opening-angle method

The opening-angle method was originally propsed by Kapelon et al.[5], and we have developed further it for our purpose on the basis of the recent data obtained by heavy-ion beam. We introduced a following quantity Θ called "reduced angle", instead of the opening-angle θ_f of the fragment directly measured,

$$\Theta = \sqrt{\frac{A_f(A_P - 1)}{A_P - A_f}}\,\theta_f, \tag{1}$$

where A_P and A_f are the masses of the projectile and the fragment, respectively. Using the reduced angle defined above, we can apply the opening-angle method for any kind of projectile and any kind of fragment (p, α, Li, ...), details of which are presented in ref. [1].

In fig. 5, we show the differential energy spectra of the silicon and iron components obtained by the opening-angle method, together with those obtained from the '89 experiment (filled symbols), where the vertical axis is multiplied by $E_0^{2.5}$. We find the iron component of '91 experiment coincides quite well with the data of '89, while the silicon data of '91 is a little bit harder than the '89 data, though the statistical errors of both experiments are large in the high energy region. One should note that there exists inevitably the detection-loss bias in the lower energy region $\lesssim$ 10 GeV/n for both components, particularly for the silicon as mentioned in sect. 1.

3.1.2. East-west asymmetry effect method

As discussed in sect. 1, we can use the terrestial mangnetic field for the estimation of the energy spectrum. In fig. 6, we present a scatter plot, $\cos\theta$ v.s. ϕ, where θ and ϕ are the zenithal and azimuthal angles of arriving particles, respectively. One finds that heavy primaries populate densely in the western half, $\phi \simeq 180° \sim 360°$, while those in the eastern half, particularly around $\phi \simeq 90°$, are rather sparce.

To see the so called "east-west asymmetry effect" more clearly, we present the azimuthal distribution of arrival cosmic-ray primaries for several ranges of the zenith angle (solid circle) in fig. 7, since the asymmetry is expected to be much more prominent

in large zenith angle than in small one. In fig. 7, we show simulated data together in the form of histogram (see Appendix A). We find the coincidence between the observed data and the simulated ones is excellent, where the azimuthal angle of experimental data is shifted in parallel along ϕ-axis by 5°, probably originated in the calibration of gondola direction just before launching. Fig. 7 indicates that the azimuthal direction of our chamber is controlled correctly as we expected.

Once confirming that the azimuthal control system of the present observation had been well functioned, we can estimate straightforwardly the *integral* energy spectra of cosmic-ray nuclei by counting the number of coming particle every direction (θ, ϕ) within a small solid angle, $\Delta \cos\theta \Delta\phi$, details of which are explained in Appendix B.

In fig. 8, we present the integral energy spectra for the silicon, sulfur, argon and calcium components (a), and the iron and sub-iron components (b). All the components show a power-like shape in the energy range $2 \sim 10$ GeV/n, and the explicit value of the exponent β for each spectrum is appeared in the figures.

Now the differential energy spectrum is straightforwardly obtained by the following relation

$$\frac{dI}{dE_0} = -\frac{\beta}{E_0} I(\geq E_0), \tag{2}$$

that is, the differential intensity at the energy E_0 is obtained by multiplying the integral flux $I(\geq E_0)$ into β/E_0, the results of which are summarized in the next subsection.

3.2 Comparison between the opening-angle and the E-W effect methods

In this section we combine the '89-data and the '91-data obtained by the opening-angle method, as the both experiments are of nearly the same condition in the chamber structure and in the observation level, except the azimuthal control, and the both data are in agreement with each other within the statistical error (see fig. 5).

In figs. 9 and 10, we summarize the differential energy spectra obtained by the both methods for the silicon and iron, and sulfur, argon and calcium, respectively. One finds the low energy data obtained by the E-W effect (filled symbols) continue smoothly to the high energy data by the opening-angle method (open symbols). One should remark further that the drop in the lower energy region due to the detection-loss bias found in the latter method, particularly for the silicon, is recovered well by the former method.

For the sub-iron components, in particular for those with $Z = 21 - 25$, we have to eliminate the contamination of fragments coming from the iron interaction in the atmosphere. While this effect was of course carefully taken into account in the previous work[1], we have imporved further and found a reasonable treatment for the *small* number of events in higher energy region, say $\gtrsim$ 100 GeV/n, details of which are discussed in Appendix C.

In fig. 11, we present the differential energy spectra for three kinds of sub-iron components, $Z = 17 - 25$, $21 - 25$ and $17 - 20$. Again we find the data of the E-W effect method continue smoothly to those of the opening-angle method, and the detection-loss bias inherent in the latter method is recovered. The present results show that the second component, $Z = 21 - 25$, is nearly 20% less than those reported in the previous work[1] in the energy region $\gtrsim$ 100 GeV/n. This is mainly because we revised the elimination procedure of fragments coming from iron as discussed in Appendix C.

3.3 Abundance ratio to iron component

The abundance ratio is important for the study of the cosmic-ray propagation in the galaxy. In particular, the sub-Fe/Fe ratio brings us the information of the escape length.

In figs. 12a and 12b, we present the abundance ratios of [Si, S, A, Ca]/Fe (a)

and [sub-Fe's]/Fe (b). One finds clearly the former ratio seems to be almost constant, independent of the the energy, while the latter decreases significantly as the energy gets higher. This means that most of the sub-iron components are created during the passage of the iron in our galaxy.

On the other hand the primary components such as the silicon and sulfur attenuate similarly as in the case of the iron, resulting in the constant abundance ratio to iron, and the calcium and argon components seem to slightly decrease with higher energy, indicating that in addition to the source origin, some of them come from the spallation of irons during the propagation through the galaxy.

4 Summary

We confirmed that the energy spectra obtained by the opening-angle method coincide satisfactorily with those obtained by the E-W effect method in the low energy region $\lesssim$ 10 GeV/n. Moreover, we find that the detection-loss bias appeared in the lower energy region for the opening-angle method is well recovered by the E-W effect method, meaning that we can get the energy spectrum in the very *wide* energy region, from a few GeV/n to a few TeV/n, with use of a *single* detector.

While we have checked the regularity of the reduced opening-angle distribution in the energy range from 1.7 GeV/n to 200 GeV/n[1], one may worry about the energy dependence of the fragmentation process in much higher energy region $\gtrsim$ 1 TeV/n. The fragmentation process is, however, essentially the low energy phenomena even in the case of very high energy projectile, looking the reaction in the mirror system. So, we can apply the opening-angle method also for the higher energy region, apart from a case that a head-on nucleus-nucleus collision occurs without producing evaporated fragments. In such a case, it would be necessary to use the psuedo-rapidity distribution of charged

pions instead of fragments (p, α, Li, ...) for the energy determination, the preliminary analysis of which is reported in ref. [6].

This paper has been focussed to only the experimental data obtained by our two balloon flights, and we don't touch on the speculation between the data and the propagational model. The preliminary analysis is appeared in ref. [7], and the full analysis will be reported soon elsewhere.

Recently, we extend our method using another type of SXF (HR-4 screen) to a new program called "RUNJOB" (RUssia-Nippon JOint Balloon program), two campaigns of which were successfully performed from Kamchatka to the western area in Russia in the summer 1995, the first one with 130 hrs exposure and the second one with 170 hrs[8]. Both exposures are approximately ten times longer than those performed in '89 and '91 experiments, and the analyses are now going on jointly with Russian group, the results of which will be reported in the near future.

Acknowledgement

We are grateful to the staff of the balloon division of Institute of Space and Astronauitical Science (ISAS), Sagamihara, Japan, for the successful flight of our chamber. We also thank the staff of emulsion division of the Institute of Cosmic Ray Research (ICRR, University of Tokyo) for valuable discussions and their helpful processing work of sensitive materials. This work was financially supported in part by ICRR (E40, 1989 and E35, 1991), and by ISAS(B50-31, 1989, and B30-61, 1991).

Appendix A

— Cutoff rigidity of cosmic-ray particle around Sanriku station —

Basic equation is given by

$$\frac{d\mathbf{R}}{dt} = \mathbf{v} \times \mathbf{B} \tag{3}$$

where $\mathbf{R}$, $\mathbf{v}$ are the rigidity and the velocity of cosmic-ray particle respectively, and $\mathbf{B}$ the geomagnetic field. It is well-known that introducing a following magnetic potential

$$U(r,\Theta,\Phi) = r_e \sum_{n=1}^{8} (\frac{r_e}{r})^{n+1} \sum_{m=0}^{n} (g_n^m \cos m\Phi + h_n^m \sin m\Phi) P_n^m(\cos\Theta), \tag{4}$$

the observational data on three components of geomagnetic field, B_r, B_Θ, B_Φ are well reproduced[9], where r_e is the earth radius, and $P_n^m(\cos\Theta)$ is the normalized Legendre function, and the numerical coefficients, g_n^m and h_n^m, are summarized in IGRF (International Geomagnetic Reference Field). In the present calculation, we use the numerical data of g_n^m and h_n^m as well as their time variation, $\dot{g}_n^m$ and $\dot{h}_n^m$, appeared in ref. [9].

From the practical point of view, we shoot a negative-charged particle with rigidity R toward the direction of (θ, ϕ) from an observational point (Θ_0, Φ_0). If the particle collides with the earth, it means the particle can not arrive at our detector. On the other hand, if it goes far away from the earth, say 30 r_e in this work, it can arrive at the detector.

The numerical calculation of eq. (3) is performed by the use of Runge-Kutta-Gill method. Since our balloon drifts slightly to the northern latitude, approximately 2° north from Sanriku station (see fig. 2), we calculate the cutoff rigidity at three observational points, Sanriku ([39.16°, 141.83°]), middle point ([40.00°, 141.50°]), and Tappi-cape ([41.18°, 140.23°]).

In fig. 13, we show some examples of numerical results on the cutoff rigidity as a function of azimuthal angle for four cases of zenith angle at middle point. One finds

that there are many fine structure of allowed belt-zone (white area) in the forbidden zone (black area), called penumbra, which have never been detected so clearly in the past calculations.

For the practical purpose, we prepare the numerical data of the cutoff energy E_c's for incident directions as many as possible, $\theta = 0°, 2°, 4°, \ldots, 90°$, and $\phi = 0°, 1°, 2°, \ldots, 359°$, that is, $E_c(i, j)$ is stored in the DISK in the form of 46×360 combinations.

Then we can perform straightforwardly the simulation calculation, starting from a random sampling of (θ, ϕ) with isotropic distribution, and next doing a sampling of primary energy E_0 with power-like spectrum. Comparing the set of these three values $(E_0; \theta, \phi)$ with the numerical data on the cutoff energy $E_c(\theta, \phi)$ stored in the DISK, we reject the particle if $E_0 < E_c$. On the other hand, if $E_0 \geq E_c$, a sampling of the interaction point in the atmosphere is subsequently performed. The fragmentation function of iron component in the atmosphere is summarized in fig. 13a of ref. [1].

We have performed the simulation calculations for three kinds of primaries, iron, calcium, and silicon, but we could not find any significant difference among these three. This is because the EW-effect depends on only the rigidity R, irrespective of the kind of nucleus, and the fragmentation process is minor effect in fig. 7 in the text.

Appendix B

— Integral energy spectrum obtained by the east-west asymmetry effect —

As illustrated in fig. 14, let us consider a case that we observe n_{ij} particles coming from the direction $[\theta_i, \phi_j]$ (hereafter called $[i, j]$-direction for the simplicity) within small solid angle $\Delta\Omega(= \Delta \cos\theta \Delta\phi)$. Of course, we know the cutoff energy E_c corresponding to the $[i, j]$-direction as presented in Appendix A. The chamber area S_i looked from the

direction of a coming particle with a zenith angle θ_i is given by

$$S_i \;=\; S\,\cos\theta_i \tag{5}$$

where S is the area of our chamber. The atmospheric thickness t_{ij} corresponding to the zenith angle θ_i is approximately expressed as

$$t_{ij} \;\simeq\; t/\cos\theta_i \tag{6}$$

though the approximation breaks slightly in large inclination, $\theta_i \gtrsim 80°$, because of the earth curvature. Now, assuming that the absolute integral intensity with energy larger than E_c is $I(\geq E_c)$ at the top of atmosphere, and the exposure time of balloon is T, we have a relation

$$S_i\Delta\Omega T\; I\; e^{-t/\Lambda\cos\theta_i} \;=\; n_{ij} \tag{7}$$

where Λ is the attenuation length of the particle in the atmosphere.

Now, let us consider a range of cutoff-energy satisfying

$$E_c \;-\; \Delta E_c \;\leq\; E_0 \;\leq\; E_c \;+\; \Delta E_c, \tag{8}$$

where ΔE_c is much less than E_c (in this work, we set $\Delta E_c/E_c = 0.06$). As shown in fig. 15, there are many $[i,j]$-sections (grey rectangles) corresponding to the cutoff energies E_0's satisfying eq. (8), and we represent its group as W. Then summing the all sections, $[i,j]$, in eq. (7), we have

$$S\Delta\Omega T I \sum_{i,j\subset W} \cos\theta_i\; e^{-t/\Lambda\cos\theta_i} \;=\; \sum_{i,j\subset W} n_{ij},$$

and finally,

$$I(\geq E_0) \;=\; \frac{1}{S\Delta\Omega T}\,\frac{\sum_{i,j\subset W}\; n_{ij}}{\sum_{i,j\subset W}\cos\theta_i\; e^{-t/\Lambda\cos\theta_i}} \tag{9}$$

In the practical calculation, we set a following small element of solid angle ($i = 1 \sim 25$, and $j = 1 \sim 90$; see fig. 15),

$$\Delta\cos\theta \;=\; 1/25 \;=\; 0.04, \quad \Delta\phi \;=\; 2\pi/90 \;=\; 0.0698\ (\text{rad.}),$$

so that

$$\Delta\Omega \;=\; \Delta\cos\theta\Delta\phi \;=\; 2.793\times10^{-3}\ (\mathrm{str.}) \tag{10}$$

Appendix C

— Elimination of fragments coming from iron interaction for sub-iron components —

In order to obtain the absolute intensity $I_i^{(0)}$ of primary i (= Fe, Mn, ..., P, Si) at the top of atmosphere, eliminating the contamination of fragment products coming from heavier primaries j ($> i$), we have to solve the following equation simultaneously,

$$\mathbf{H}\cdot\mathbf{I}^{(0)} \;=\; \mathbf{I}^{(obs)}, \tag{11}$$

where $\mathbf{I}^{(obs)}$ is the intensity at the observation level with 13 components, $(I_1^{(obs)}, I_2^{(obs)}, \ldots, I_{13}^{(obs)}) \equiv (I_{Fe}^{(obs)}, I_{Mn}^{(obs)}, \ldots, I_{Si}^{(obs)})$, and

$$H_{ij} = (\nu_j\kappa_j\eta_{ij}e^{-t/\lambda_i}) \quad \text{with } H_{ij}=0 \ \text{ for } i<j, \tag{12}$$

ν_j relates to the charge resolution, and κ_j to the chambr efficiency, and η_{ij} to both the fragmentation parameter P_{ij} and the collision mean free paths λ_i, λ_j, details of which are summarized in ref. [1].

In the previous work, we solved eq. (11) simultaneously by the use of a Gauss-Jordan method, and summed each sub-iron component at the top of atmosphere, for instance in the case of the group X: Z=21-25,

$$I_X^{(0)} \;=\; \sum_{i=2}^{6} I_i^{(0)}. \tag{13}$$

This method causes, however, a problem that we often face a negative flux value for some constituent element in the group X, particularly for manganese ($Z=25$), while the superposed flux $I_X^{(0)}$ gives a reasonable positive value. It is natural that such an unrealistic result occurs at some energy-bin with *zero* event for Mn, the element just one

charge unit less than the iron. Whereas, the negative value appeared in Mn raises the flux at the same energy-bin for the next lighter element, Cr($Z = 24$). Nevertheless, we have used eq. (13) to get sub-iron component in the previous work, presuming that the above problems would be cancelled each other.

After the previous work, we have investigated this problem further, and found that for small number of events, corresponding to high energy region, eq. (13) gives a little bit higher values than the true one. To settle this problem, we find a following method. That is, instead of eq. (13), we combine *in advance* the sub-iron group for each observed energy spectrum, that is

$$I_X^{(obs)} = \sum_{i=2}^{6} I_i^{(obs)}, \tag{14}$$

and we regard this group X as a second observed element, $i = 2$, in eq. (11). We make further a following combination in eq. (11),

$$\sum_{i=2}^{6} H_{ij} I_i^{(0)} = \bar{H}_{X,j} I_X^{(0)}, \tag{15}$$

where

$$\bar{H}_{X,j} = \sum_{i=2}^{6} H_{ij} \tau_i^{(0)} \quad \text{with} \quad \tau_i^{(0)} = I_i^{(0)} / I_X^{(0)}. \tag{16}$$

We can regard $\bar{H}_{X,j}$ as an averaged transition parameter for the fragmentation process X-group $\rightarrow$ j-element, with the weight of a fraction rate of each constituent element in the X-group.

Practically, the fraction of i-element in the X-group is approximately set as

$$\tau_i^{(0)} \simeq \tau_i^{(obs)} \equiv \bar{I}_i^{(obs)} / \bar{I}_X^{(obs)}, \tag{17}$$

where $\bar{I}_i^{(obs)}$ and $\bar{I}_X^{(obs)}$ are obtained by fitting a straight line to the observed energy spectra, $I_i^{(obs)}$ and $I_X^{(obs)}$ with use of the least square method, respectively. This replacement causes only a few % diffrence in the final solution, based on the simulation calculation.

This procedure is reasonable also from the fact that the charge resolution is poor for individual sub-iron elements, particularly for manganese, while the purity of the combined group is satisfactory enough, for instance $[21\text{-}25]_{obs}/[21\text{-}25]_{true} \sim 85$ % in this work (see ref. [1] for detail).

References

[1] M. Ichimura et al., Phys. Rev. D48 (1993) 1949.

[2] M. Ichimura et al., Nucl. Instrum. Methods A 300 (1991) 374.

[3] T. Hayashi and T. Doke, Nucl. Instrum. Methods 174 (1980) 349.

[4] For instance, see J. Nishimura et al., Adv. Space Res. (Pergamon Press) 1 (1981) 127.

[5] M.F. Kaplon et al., Phys. Rev. 85 (1952) 296.

[6] H. Nanjo et al., in Proc. 24th Int. Cosmic Ray Conf., Rome (1995), vol. 3, p. 697.

[7] M. Ichimura et al., in Proc. 24th Int. Cosmic Ray Conf., Rome (1995), vol. 3, p. 104;
T. Shibata, Rapporteur Talk presented at the 24th Int. Cosmic Ray Conf., Rome (1995) (to be published in Il Nuovo Cimento).

[8] S.I. Nikolsky et al., in Proc. 24th Int. Cosmic Ray Conf., Rome (1995), vol. 3, p. 571.

[9] Numerical Table of Physical Geography, published by National Astronomical Observatory, Japan (1990), p. 796.

Fugure captions

1. Chamber design of the present work. SP: spacer (styrofoam) with 2mm thickness, SXF: screen-type X-ray film, Em A: acrylic target with 1mm thickness, coated with 50 μm nuclear emulsion (Fuji ET7B-type) on the upper surface, Em B and Em C: nuclear emulsion plate with 500 μm acrylic base, coated with 55 μm nuclear emulsion (Fuji ET7B-type) on both sides, where in some of Em B's, ET6B-type nulcear emulsion (low sensitive) is coated at the lower surface.

2. Trajectory of our balloon. The balloon was drifted to the northern latitude by $\sim 2°$.

3. Accuracy of the azimuthal control of the gondola.

4. Charge spectrum of heavy cosmic-ray priamries passing through the trigger layer.

5. Differential energy spectra of the silicon and iron components obtained by the opening-angle method, where the vertical axis is multiplied by $E_0^{2.5}$.

6. Scatter plot of $\cos\theta$ v.s. ϕ for the heavy primaries detected by SXF.

7. Azimuthal distribution of arriving cosmic-ray heavy primaries (solid circles) for five ranges of the zenith angle. Simulated data are also shown in the form of histogram.

8. Integral energy spectra for several kinds of elements. β is the value of exponent when we fit each spectrum by a straight line.

9. Differential energy spectra of the silicon and iron components obtained by the E-W effect method (filled symbols) and the opening-angle method (open symbols), where the '89 and the '91 data are combined in the case of the latter method.

10. Same figure as fig. 9, but for the sulfur, argon and calcium components.

11. Same figure as fig. 9, but for three kinds of sub-iron components.

12. Abundance ratios of [Si, S, A, Ca]/iron (a) and [sub-iron]/iron (b).

13. Cutoff rigidity at [E, W] = [40.0°, 141.5°], a middle point between the launching

place, [39.2°, 141.8°] (Sanriku), and the landing place, [41.2°, 140.2°] (Tappi-cape).

14. Illustration of the relation between the absolute intensity at the top of the atmosphere $I(\geq E_{cut})$ and the observed number of cosmic rays n_{ij} coming from a direction (θ_i, ϕ_j) within a small solid angle $\Delta\Omega$ at our chamber.

15. Diagram of $\cos\theta$ v.s. ϕ, each divided into 25 and 90 sections, respectively, where n_{ij} is the number of cosmic-ray primaries coming from the direction (θ_i, ϕ_j) within the solid angle $\Delta\Omega \equiv \Delta\cos\theta\Delta\phi$. Grey rectangles represent the same group having the cutoff energies E_0's with $E_c - \Delta E_c \leq E_0 \leq E_c + \Delta E_c$.

Table captions

1. Flight performance of two experiments.

2. Statistics of individual elements passing through the trigger layer, and the number of events interacting with the target. '89-data are also presented.

3. Summary of the event number performing emission-angle measurement of fragment particles using microscope. '89-data are also presented.

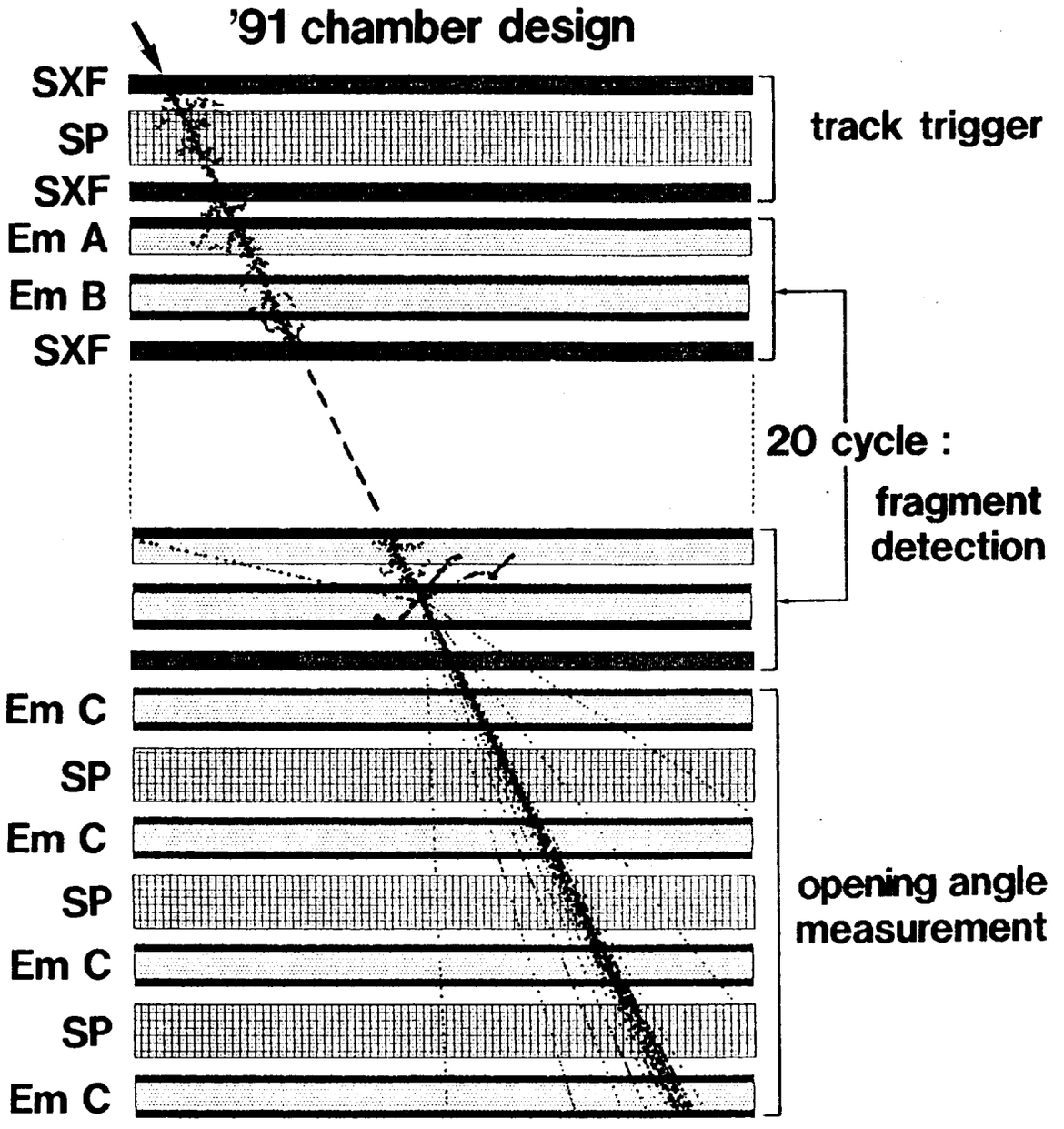
'91 chamber design
SXF
SP
SXF
Em A
Em B
SXF
track trigger
20 cycle :
fragment
detection
Em C
SP
Em C
SP
Em C
SP
Em C
opening angle
measurement

Fig. 1

Fig. 2

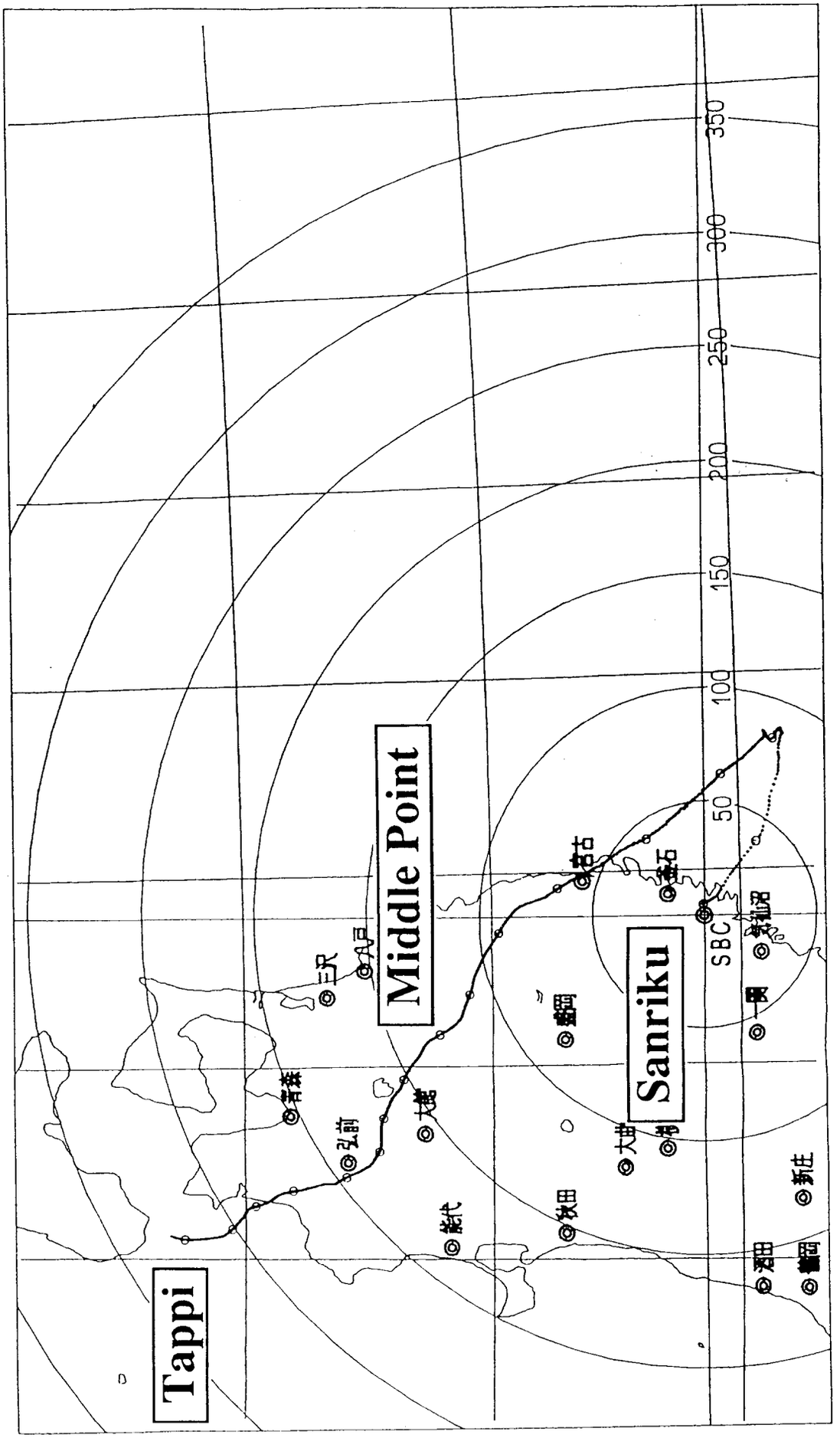
Tappi
Middle Point
Sanriku
SBC
50
100
150
200
250
300
350
青森
弘前
大館
能代
秋田
横手
大曲
花巻
北上
釜石
宮古
盛岡
一関
気仙沼
石巻
仙台
福島

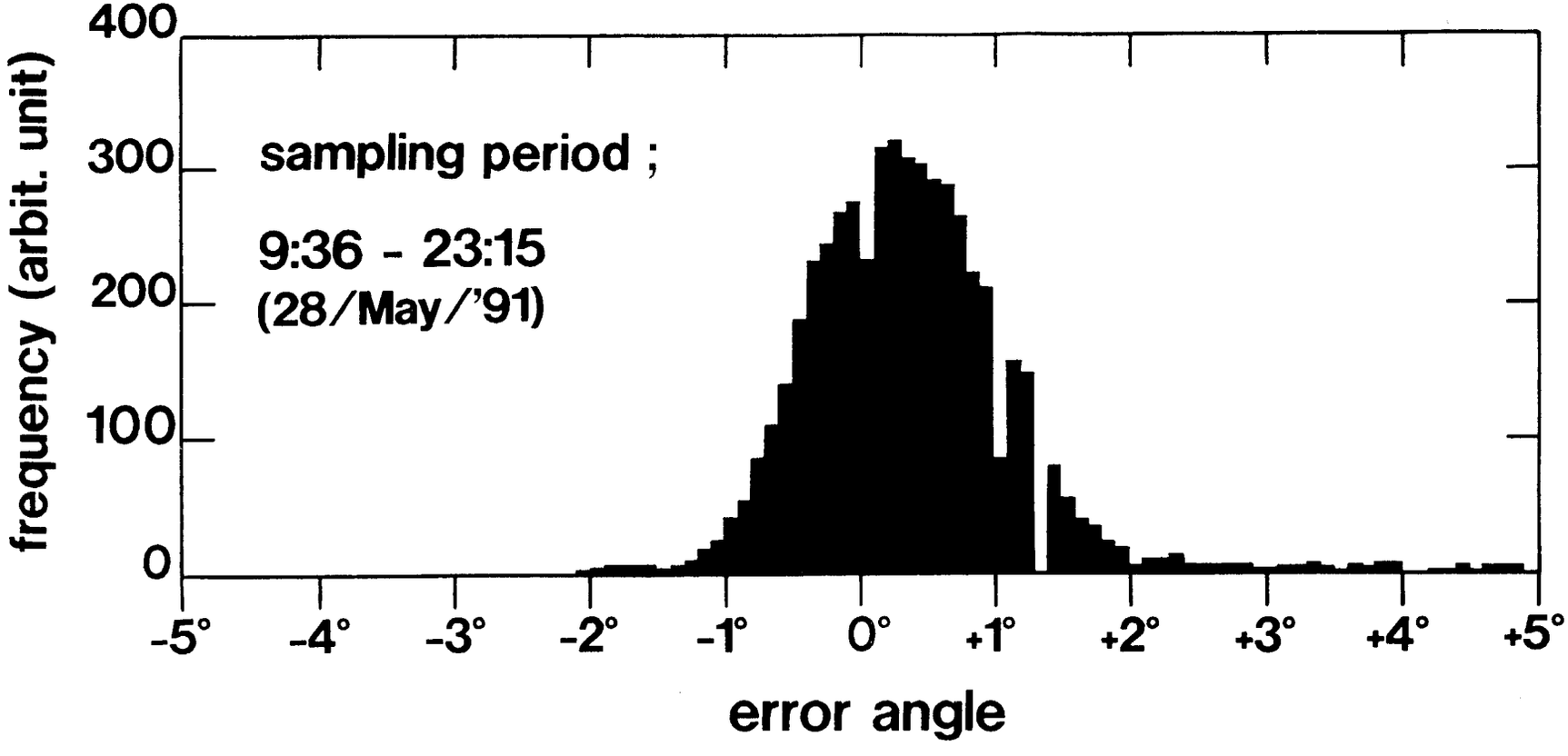
400
300
200
100
0
frequency (arbit. unit)
sampling period ;
9:36 - 23:15
(28/May/'91)
-5°
-4°
-3°
-2°
-1°
0°
+1°
+2°
+3°
+4°
+5°
error angle

Fig. 3

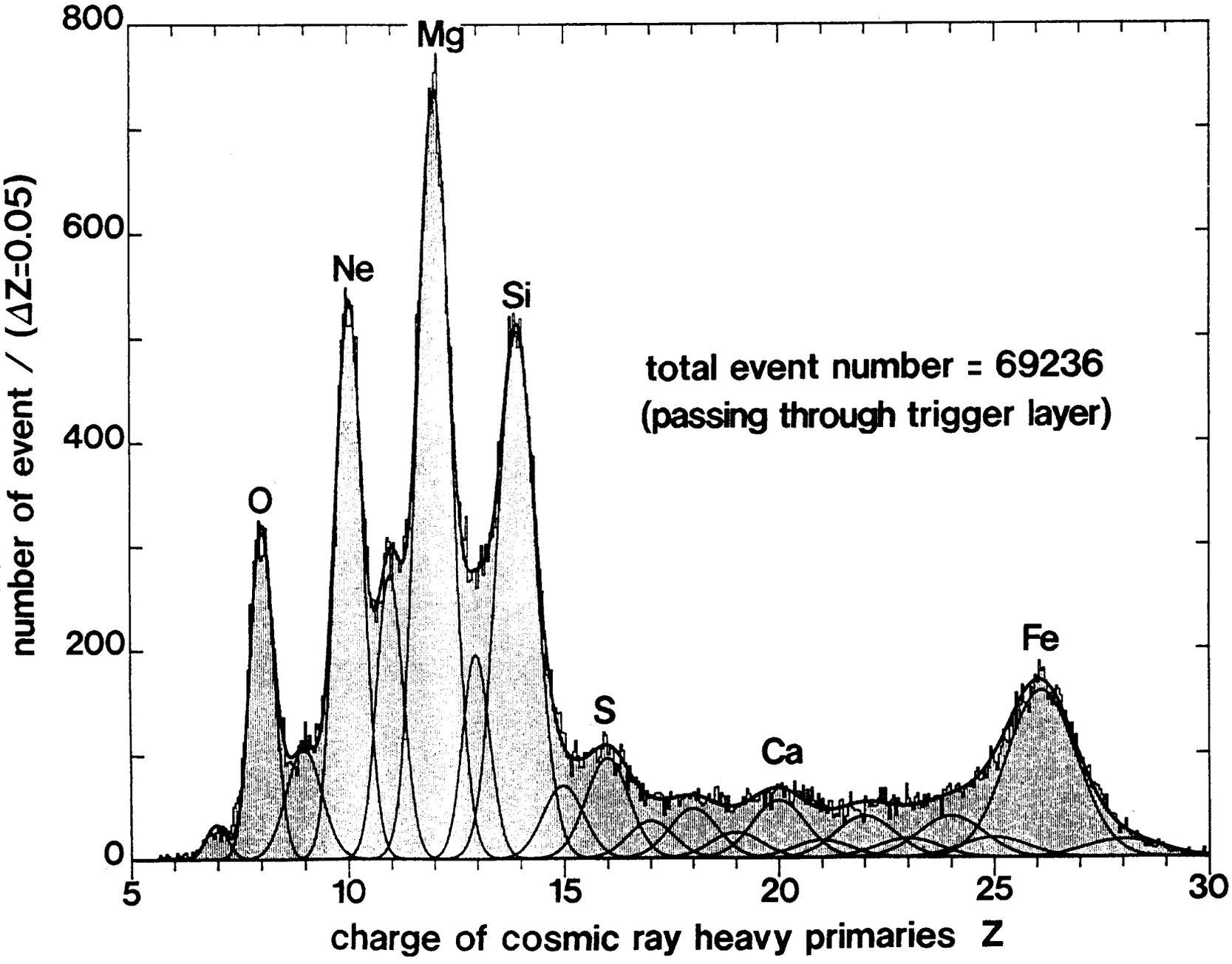
800
600
400
200
0
Mg
Ne
Si
O
S
Ca
Fe
total event number = 69236
(passing through trigger layer)
number of event / (ΔZ=0.05)
5
10
15
20
25
30
charge of cosmic ray heavy primaries Z

Fig. 4

Fig. 5

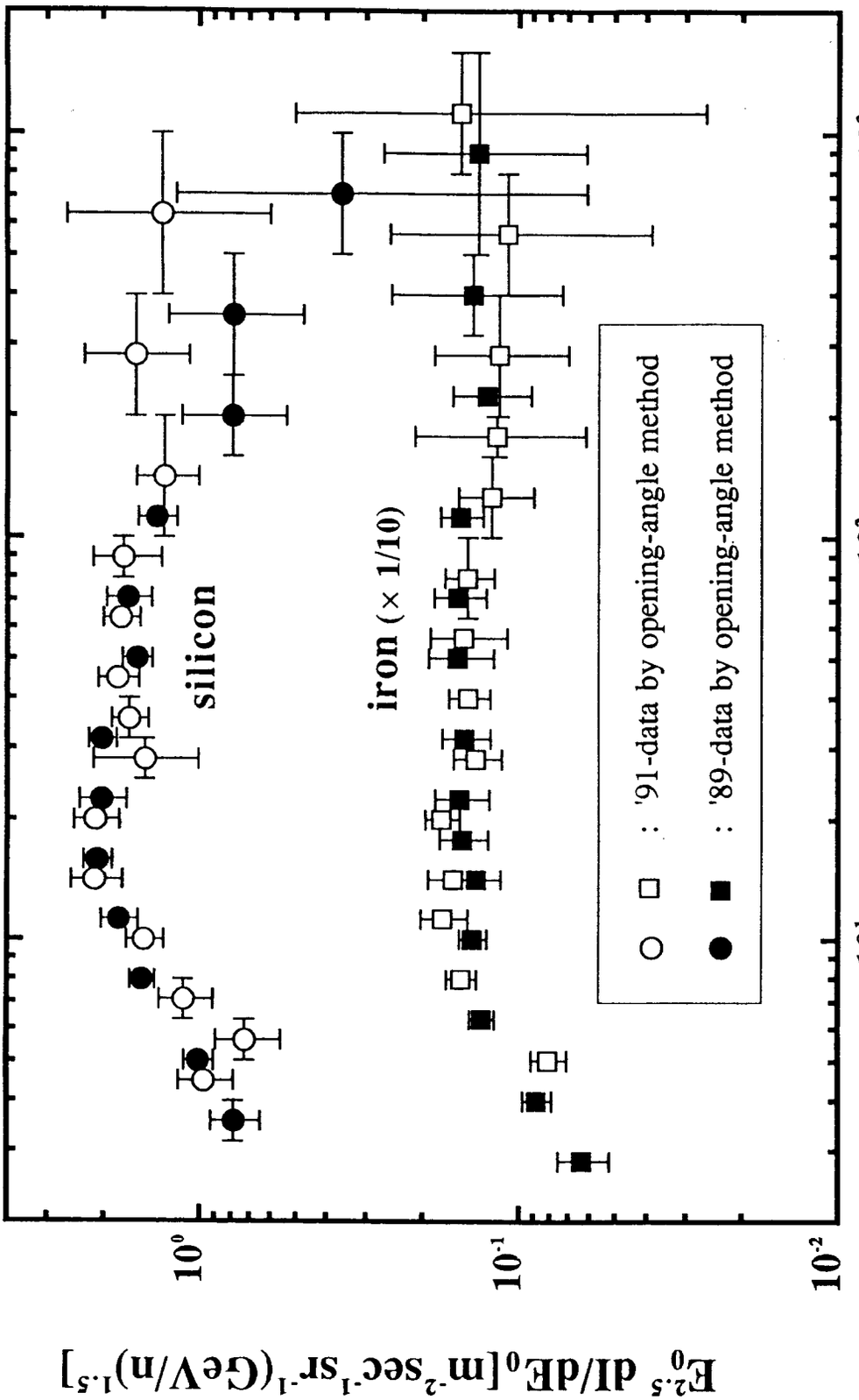
silicon
iron (× 1/10)
: '91-data by opening-angle method
: '89-data by opening-angle method
$E_0^{2.5}$ dI/dE$_0$ [m^{-2}sec^{-1}sr^{-1}(GeV/n)$^{1.5}$]
kinetic energy E_0 (GeV/n)

Fig. 6

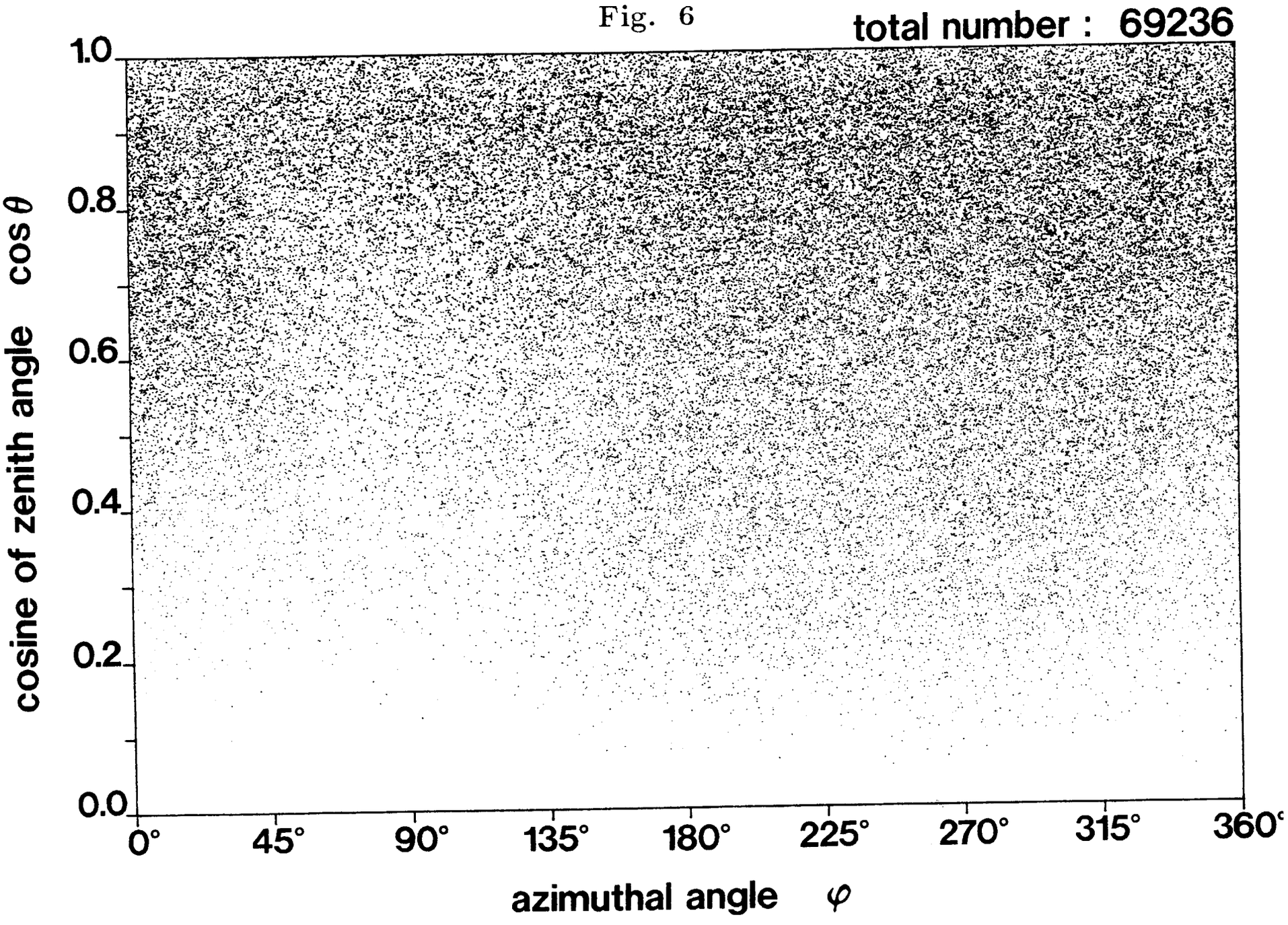
total number : 69236
1.0
0.8
0.6
0.4
0.2
0.0
cosine of zenith angle cos θ
0°
45°
90°
135°
180°
225°
270°
315°
360°
azimuthal angle φ

Fig. 7

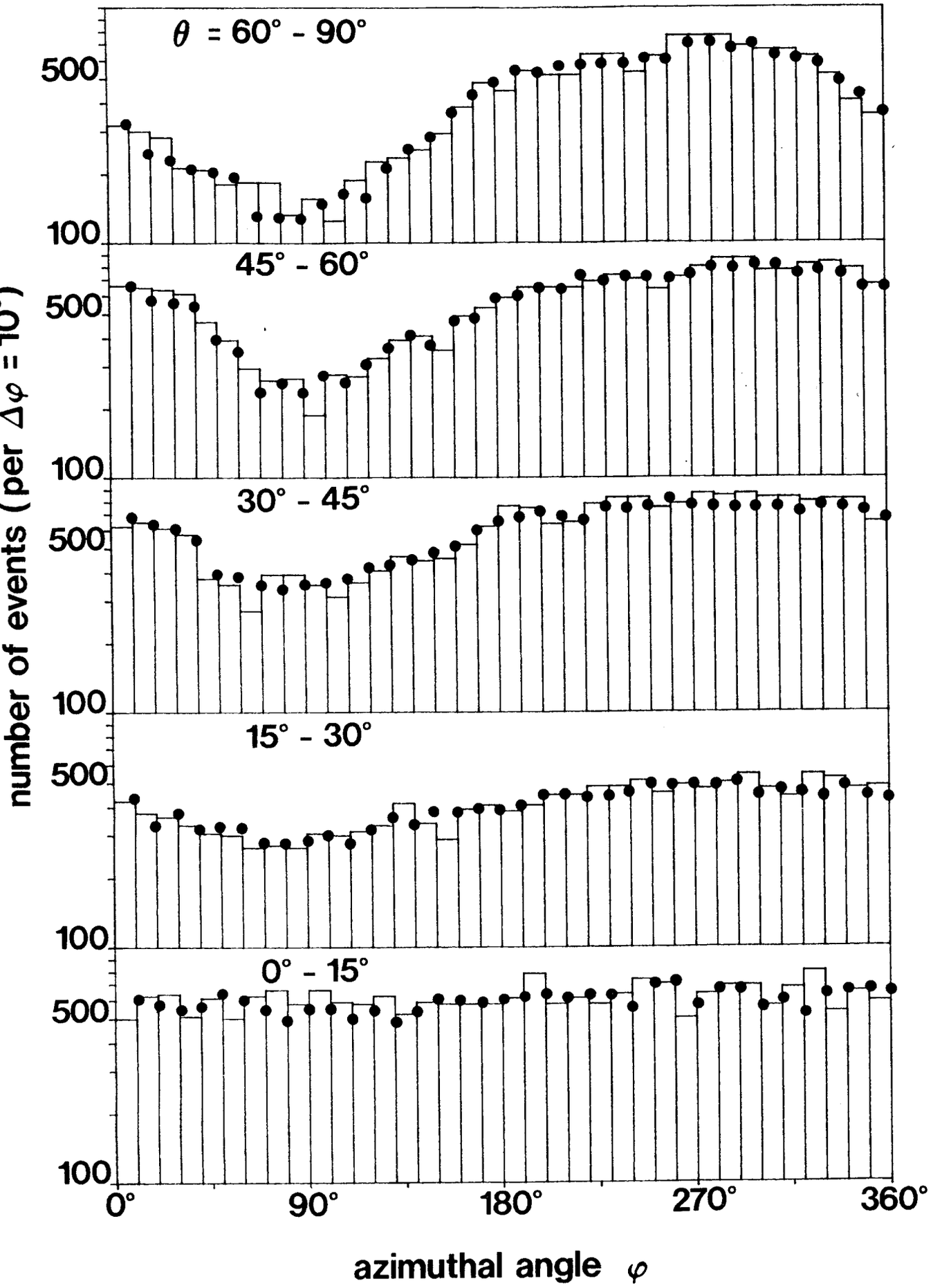
θ = 60° - 90°
45° - 60°
30° - 45°
15° - 30°
0° - 15°
500
100
number of events (per Δφ = 10°)
0°
90°
180°
270°
360°
azimuthal angle φ

Fig. 8a

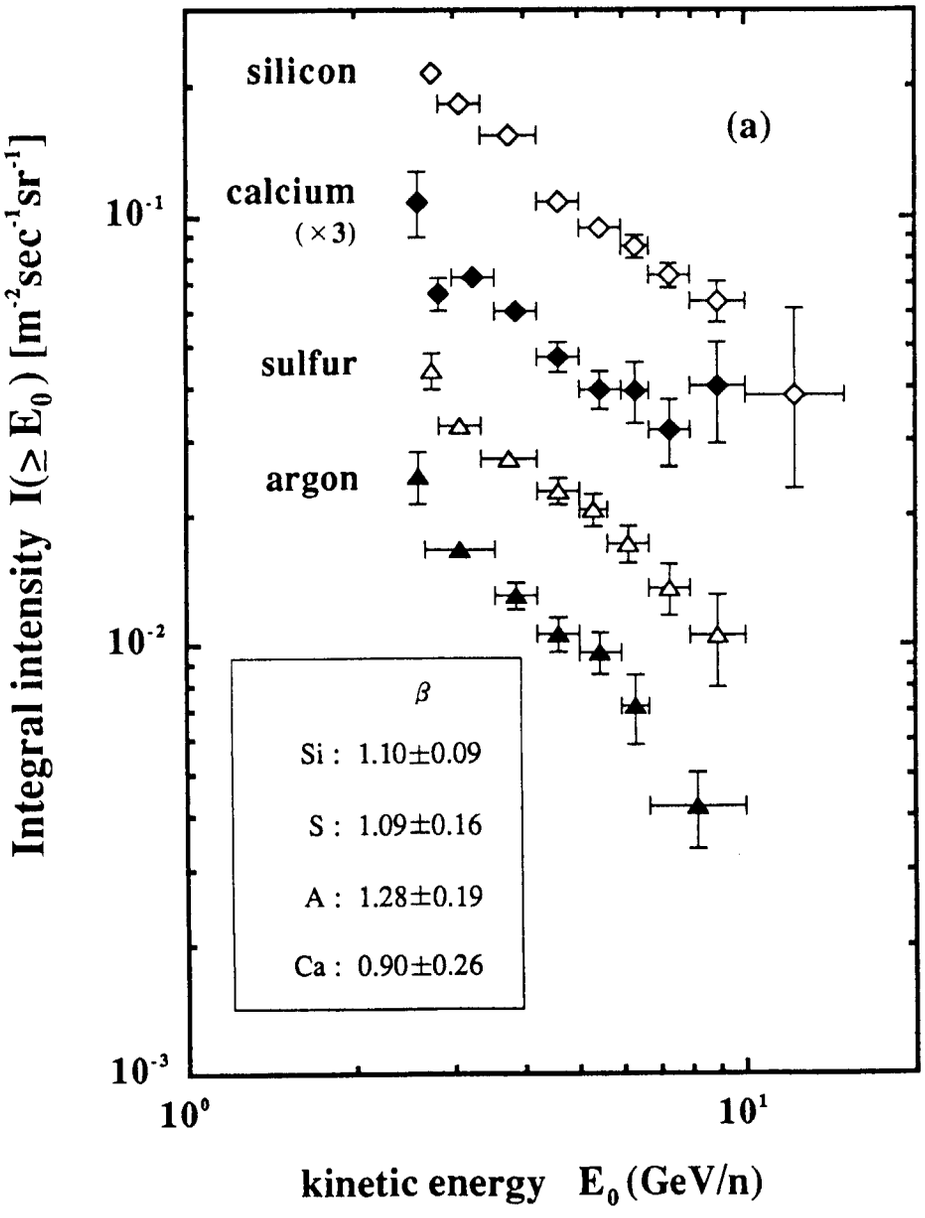
silicon
(a)
calcium
(×3)
sulfur
argon
β
Si : 1.10±0.09
S : 1.09±0.16
A : 1.28±0.19
Ca : 0.90±0.26
Integral intensity I(≥ E0) [m-2sec-1sr-1]
kinetic energy E0 (GeV/n)

Fig. 8b

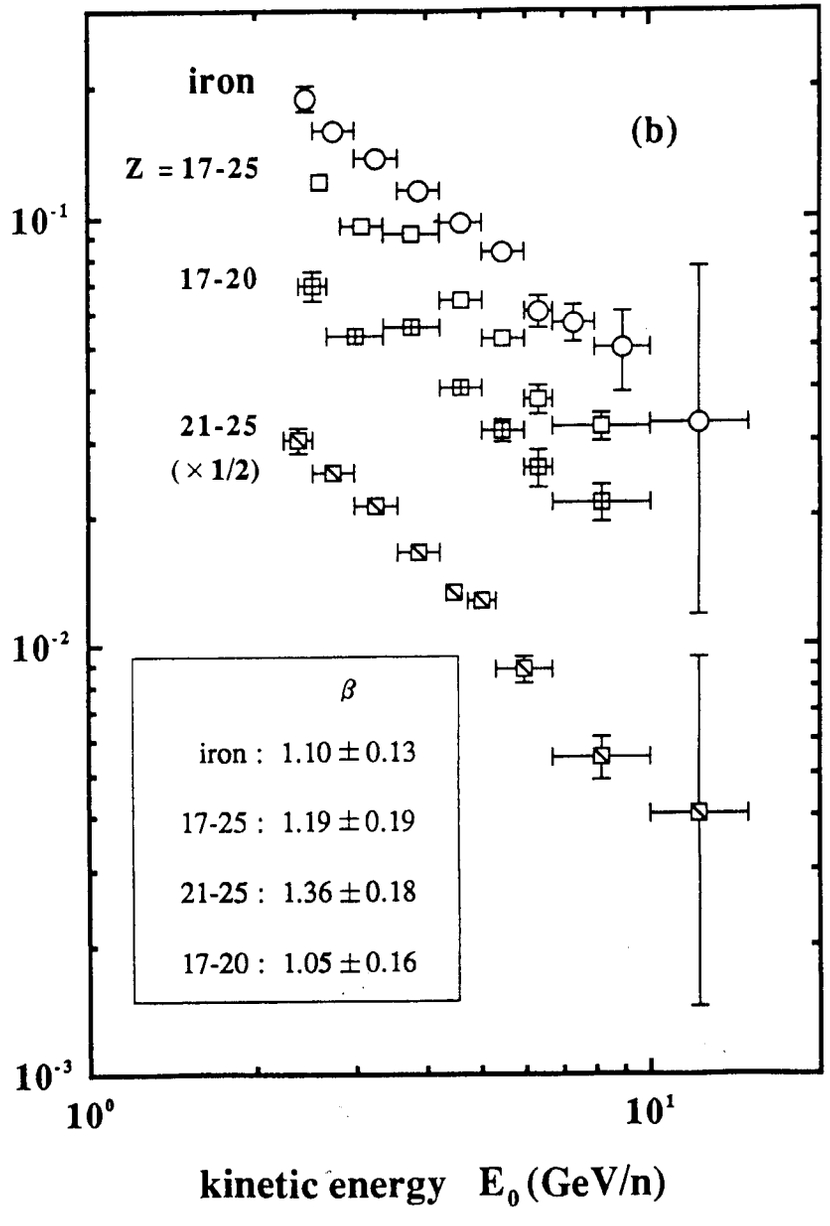
iron
(b)
Z = 17-25
17-20
21-25
(× 1/2)
β
iron : 1.10 ± 0.13
17-25 : 1.19 ± 0.19
21-25 : 1.36 ± 0.18
17-20 : 1.05 ± 0.16
kinetic energy E0 (GeV/n)

Fig. 9

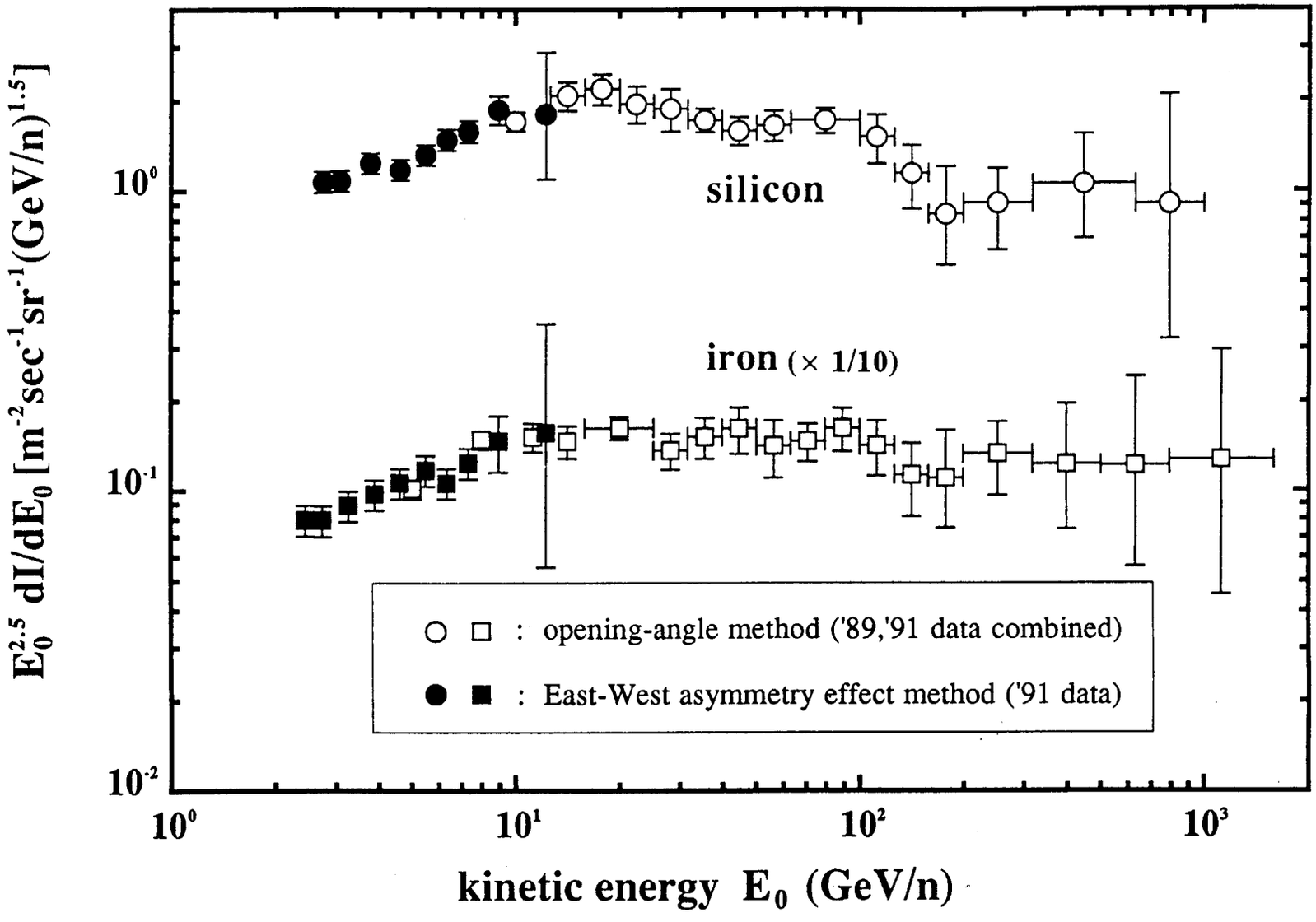
$E_0^{2.5}$ dI/dE$_0$ [m^{-2}sec^{-1}sr^{-1}(GeV/n)$^{1.5}$]
10^0
10^{-1}
10^{-2}
silicon
iron (× 1/10)
○ □ : opening-angle method ('89,'91 data combined)
● ■ : East-West asymmetry effect method ('91 data)
10^0
10^1
10^2
10^3
kinetic energy E$_0$ (GeV/n)

Fig. 10

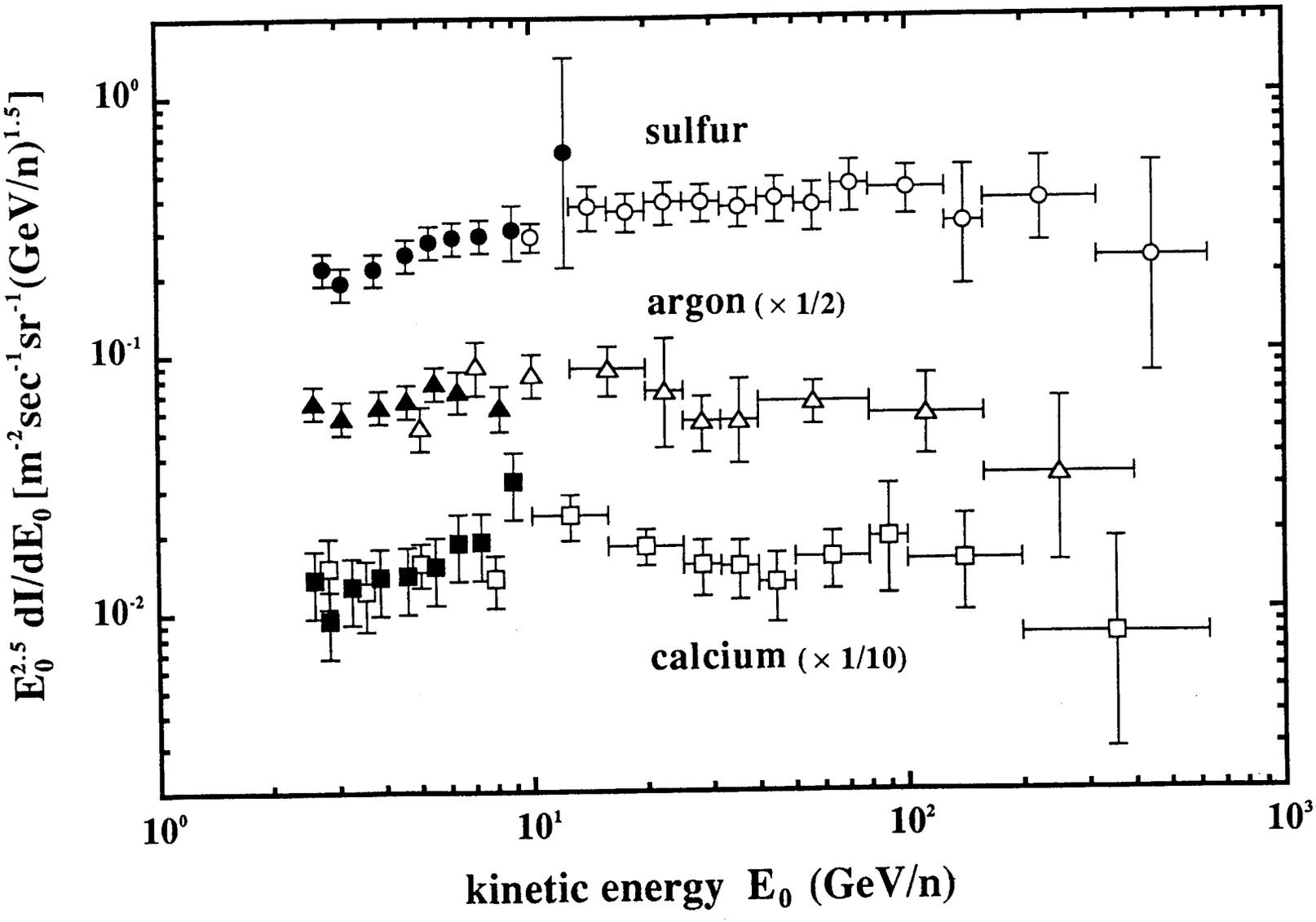
sulfur
argon (× 1/2)
calcium (× 1/10)
$E_0^{2.5}$ dI/dE$_0$ [m^{-2}sec^{-1}sr^{-1}(GeV/n)$^{1.5}$]
kinetic energy E$_0$ (GeV/n)
10^0
10^{-1}
10^{-2}
10^1
10^2
10^3

Fig. 11

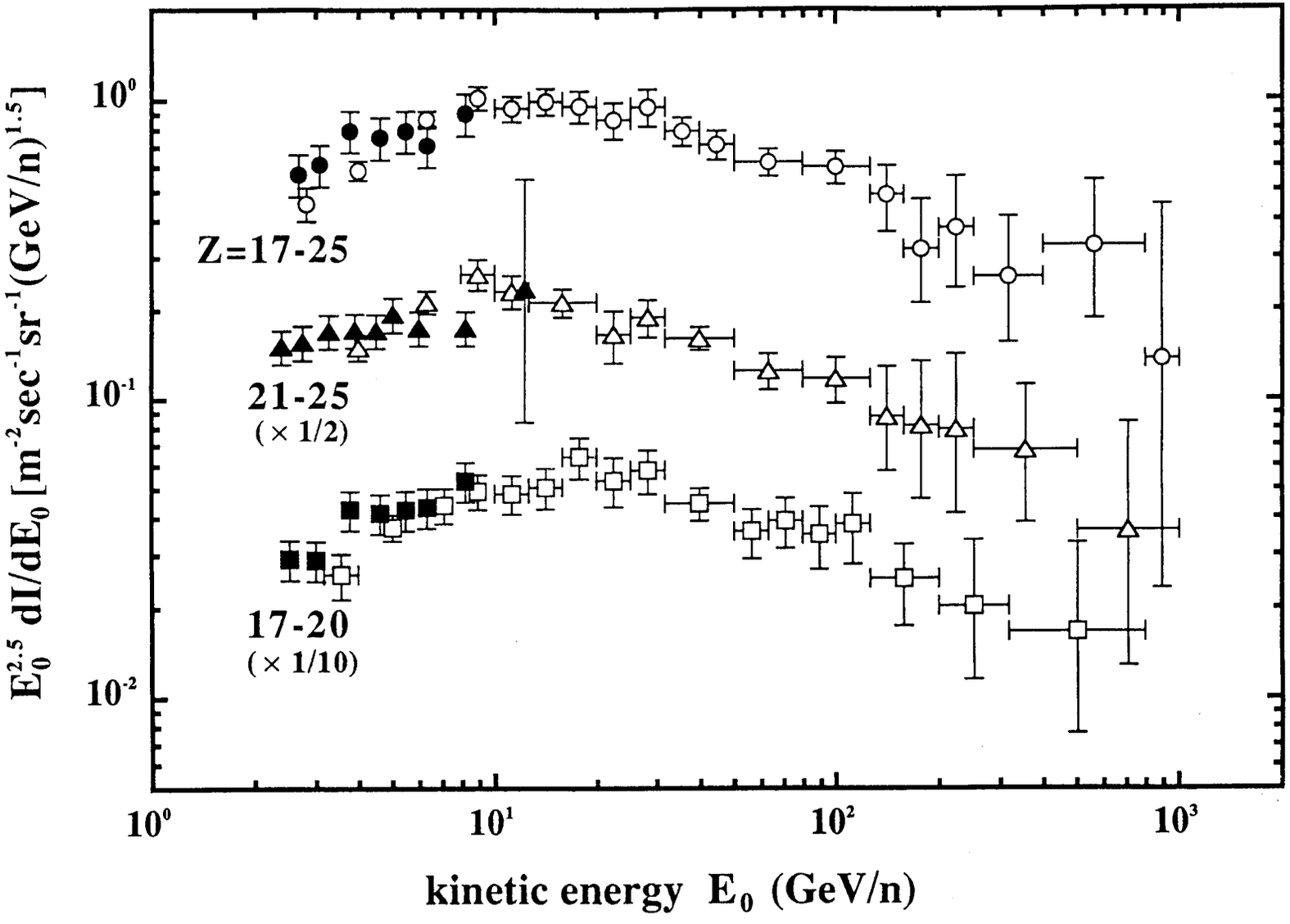
$E_0^{2.5}$ dI/dE$_0$ [m^{-2}sec^{-1}sr^{-1}(GeV/n)$^{1.5}$]
10^0
10^{-1}
10^{-2}
Z=17-25
21-25
(× 1/2)
17-20
(× 1/10)
10^0
10^1
10^2
10^3
kinetic energy E$_0$ (GeV/n)

Fig. 12a

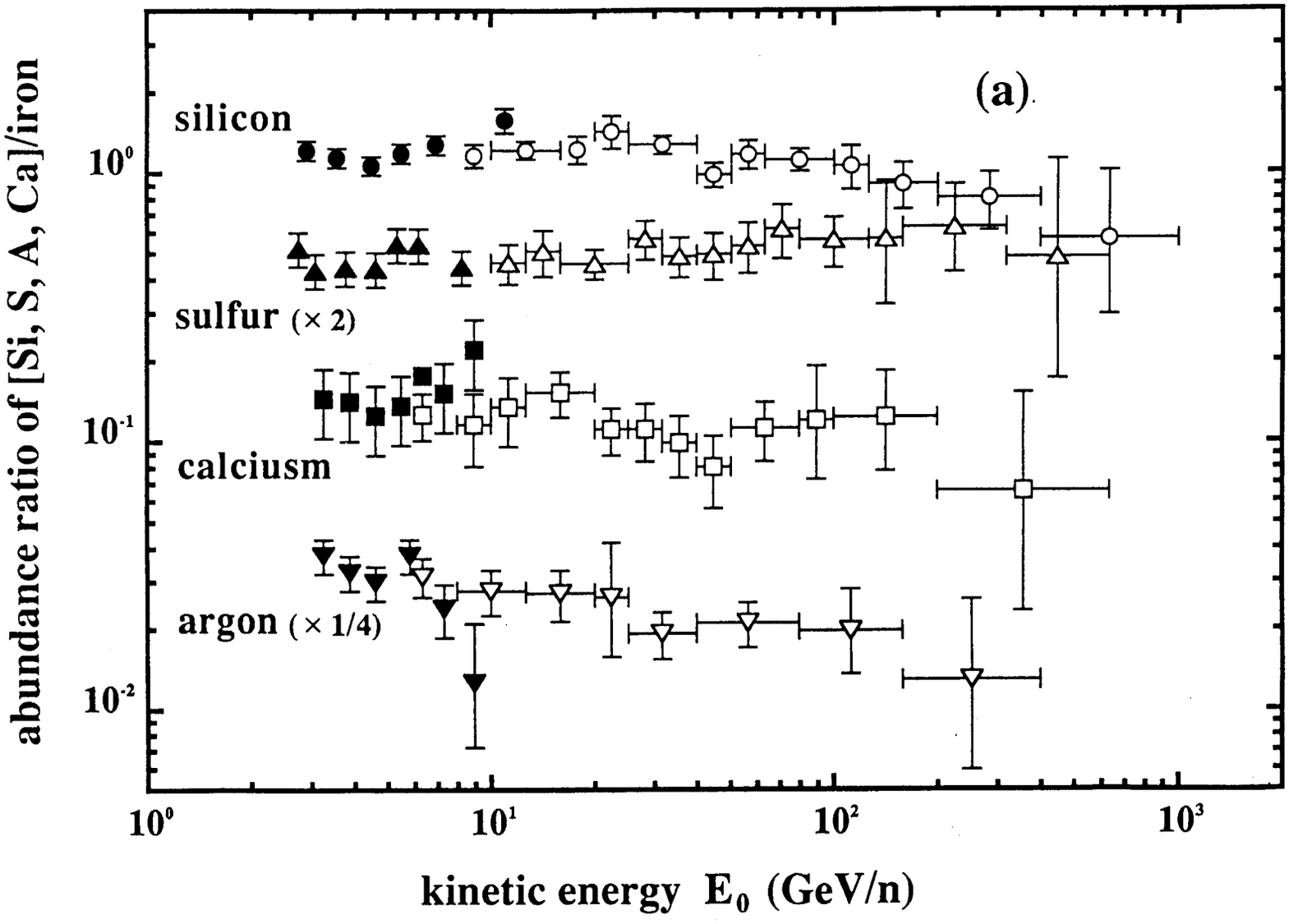
(a)
silicon
sulfur (× 2)
calciusm
argon (× 1/4)
abundance ratio of [Si, S, A, Ca]/iron
kinetic energy E_0 (GeV/n)
10^0
10^{-1}
10^{-2}
10^0
10^1
10^2
10^3

Fig. 12b

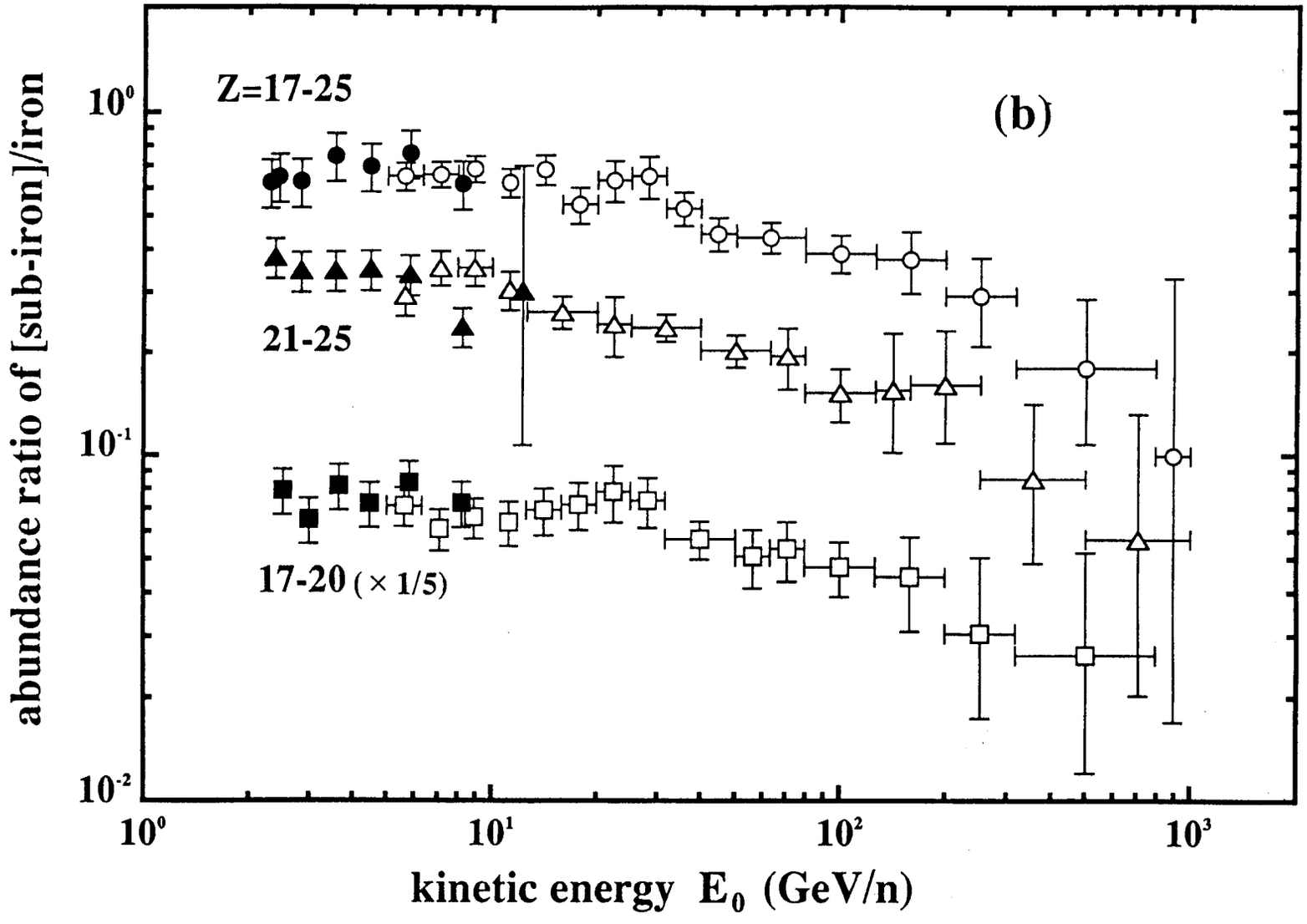
Z=17-25
(b)
21-25
17-20 (× 1/5)
abundance ratio of [sub-iron]/iron
kinetic energy E0 (GeV/n)
10^0
10^-1
10^-2
10^0
10^1
10^2
10^3

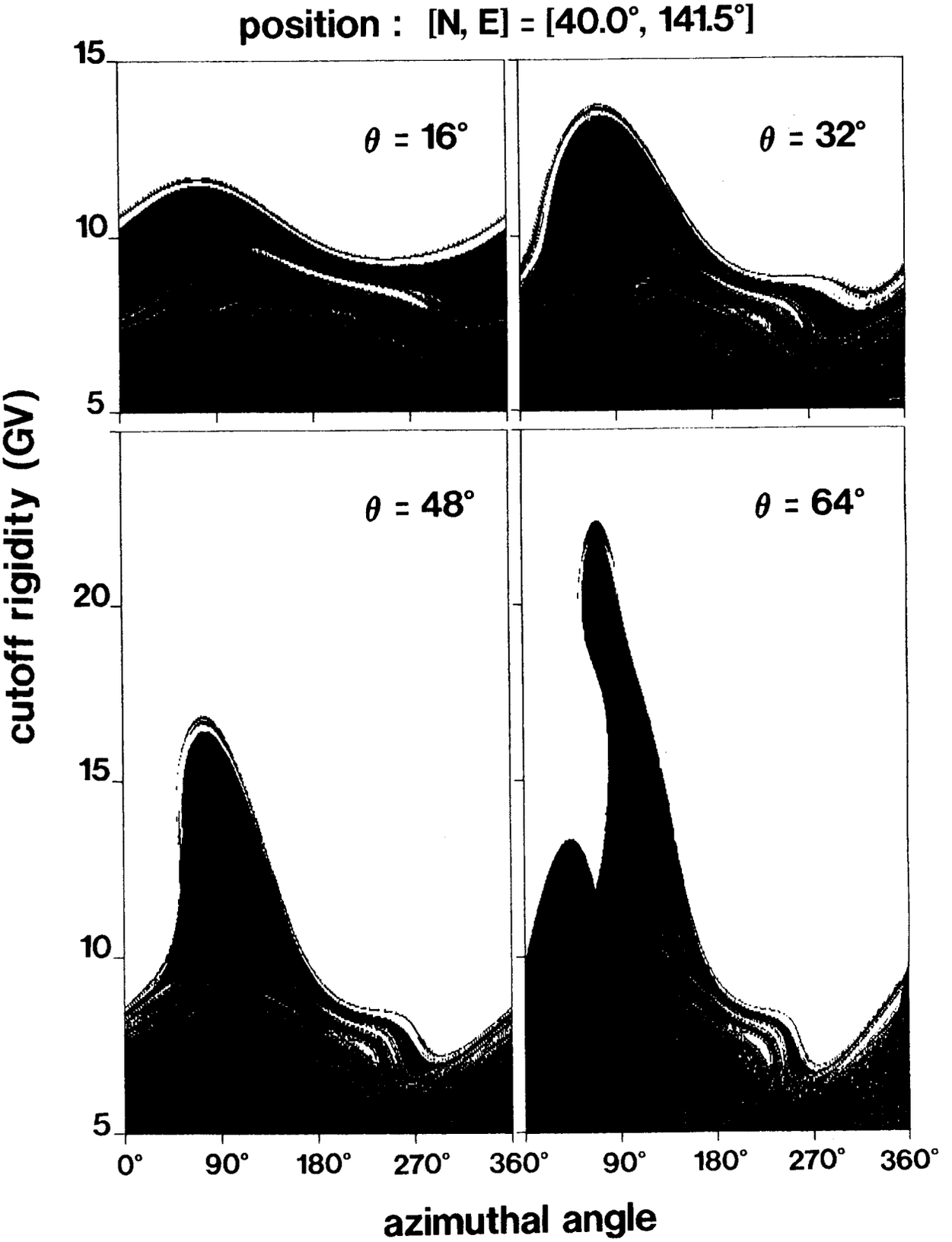
position : [N, E] = [40.0°, 141.5°]
θ = 16°
θ = 32°
θ = 48°
θ = 64°
cutoff rigidity (GV)
15
10
5
20
15
10
5
0°
90°
180°
270°
360°
90°
180°
270°
360°
azimuthal angle

Fig. 13

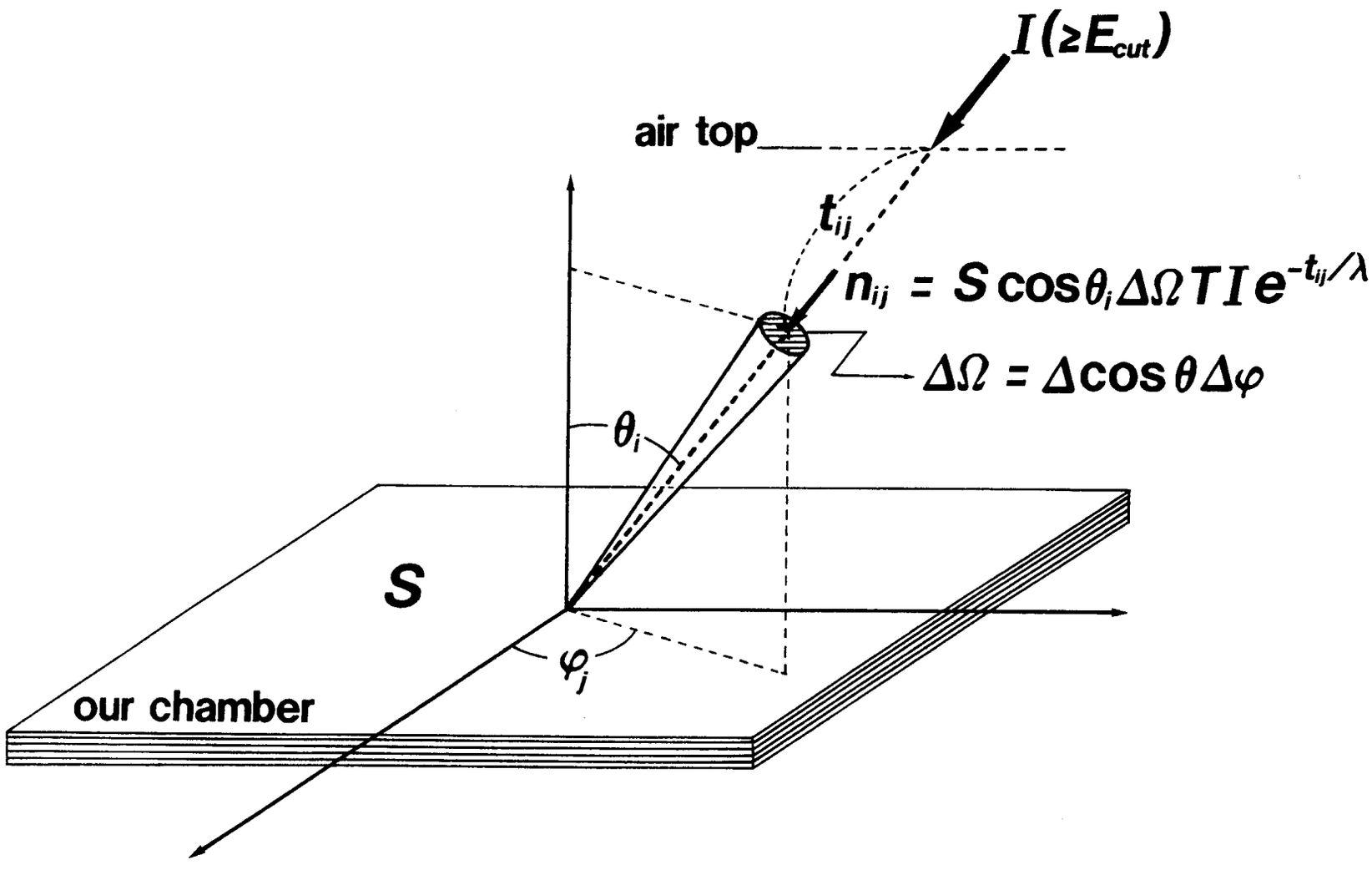
$I(\geq E_{cut})$
air top
t_{ij}
$n_{ij} = S\cos\theta_i \Delta\Omega T I e^{-t_{ij}/\lambda}$
$\Delta\Omega = \Delta\cos\theta\Delta\varphi$
θ_i
S
φ_j
our chamber

Fig. 14

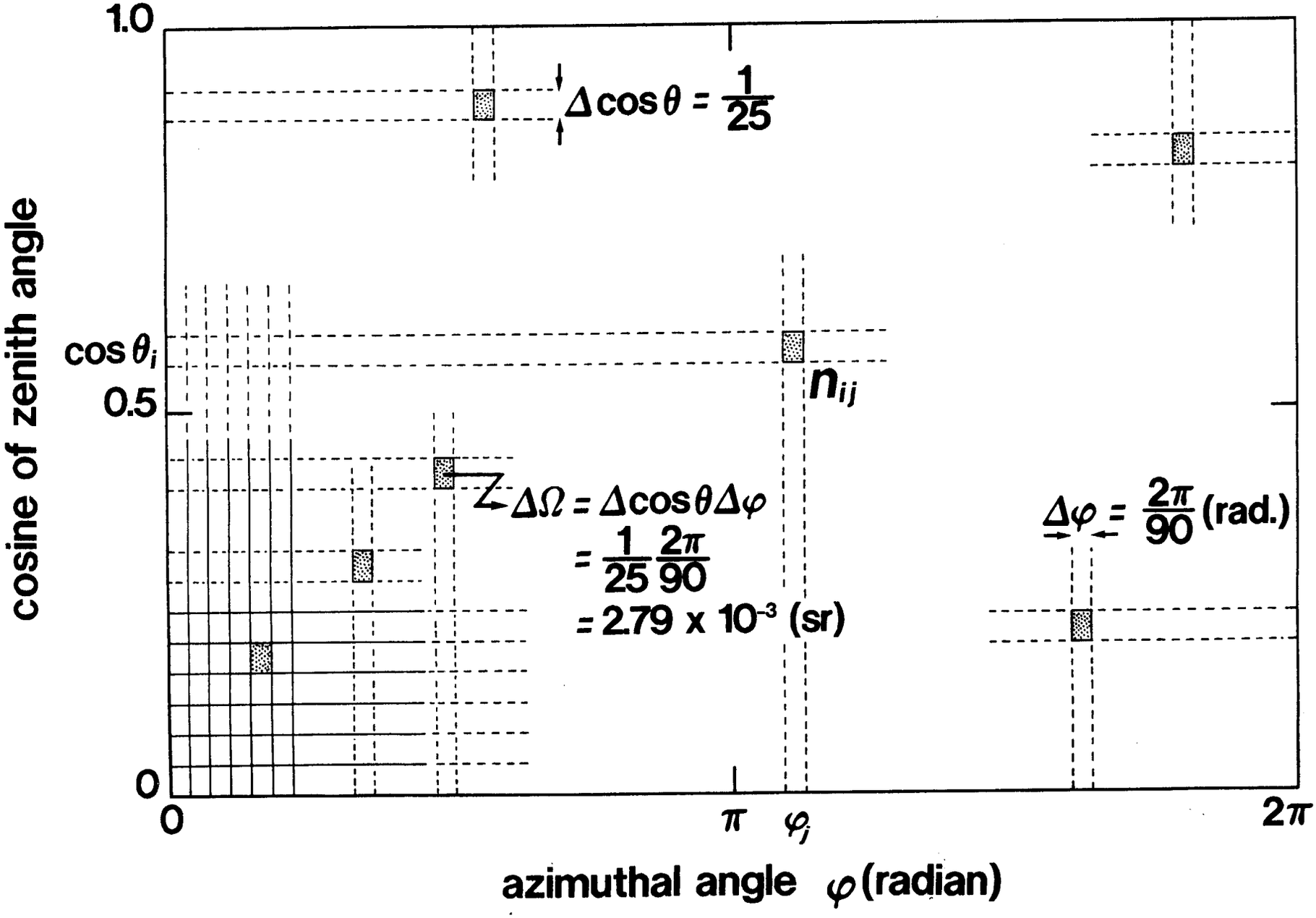
1.0
$\Delta\cos\theta = \frac{1}{25}$
cosine of zenith angle
$\cos\theta_i$
0.5
n_{ij}
$\Delta\Omega = \Delta\cos\theta\Delta\varphi$
$= \frac{1}{25}\frac{2\pi}{90}$
$= 2.79 \times 10^{-3}$ (sr)
$\Delta\varphi = \frac{2\pi}{90}$ (rad.)
0
0
π
φ_j
2π
azimuthal angle φ (radian)

Fig. 15

Table 1.

Launch date	May 25,1989	May 28,1991
Exposure time [h]	22.2	15.8
Chamber area [m^2]	1.53	1.22
Altitude [g/cm^2]	11.7	8.9
Weight [kg]	200	150

Table 2.

Charge range	Primary	Number of jets occured within the target layer		Number of events passing through the trigger layer	
		1989	1991	1989	1991
13.5－14.5	Silicon	3492	2688	11533	8188
15.5－16.5	Sulfur	952	714	2977	1927
17.0－25.0	Sub-iron	4840	3421	11754	9293
≧25.0	Iron group	2696	2122	9527	6968

Table 3.

Charge range	1989	1991
13.5－14.5	1187	708
15.5－16.5	522	251
17.0－25.0	1753	726
≧25.0	1013	545